Available online at www.sciencedirect.com

ScienceDirect

Journal of Magnesium and Alloys 12 (2024) 159–170

www.elsevier.com/locate/jma

Full Length Article

Superconducting joints using reacted multifilament MgB_2 wires: A technology toward cryogen-free MRI magnets

Dipak Patel[a,b,1,*], Akiyoshi Matsumoto[b,*], Hiroaki Kumakura[b], Yuka Hara[b], Toru Hara[b], Minoru Maeda[c], Hao Liang[a], Yusuke Yamauchi[d,e], Seyong Choi[c], Jung Ho Kim[f], Md Shahriar A. Hossain[a]

[a] *School of Mechanical and Mining Engineering, The University of Queensland, St Lucia, Queensland 4072, Australia*
[b] *National Institute for Materials Science (NIMS), 1-2-1 Sengen, Tsukuba, Ibaraki 305-0047, Japan*
[c] *Department of Electrical Engineering and Kangwon High Magnetic Field Center, Institute of Quantum Convergence Technology, Kangwon National University, Gangwon 24341, Republic of Korea*
[d] *Australian Institute for Bioengineering and Nanotechnology (AIBN), The University of Queensland, St Lucia, Queensland 4072, Australia*
[e] *Department of Materials Process Engineering, Graduate School of Engineering, Nagoya University, Nagoya, Aichi 464-8603, Japan*
[f] *Institute for Superconducting and Electronic Materials, Australian Institute for Innovative Materials, University of Wollongong, North Wollongong, New South Wales 2500, Australia*

Received 14 August 2023; received in revised form 25 October 2023; accepted 13 November 2023
Available online 23 January 2024

Abstract

The development of superconducting joining technology for reacted magnesium diboride (MgB_2) conductors remains a critical challenge for the advancement of cryogen-free MgB_2-based magnets for magnetic resonance imaging (MRI). Herein, the fabrication of superconducting joints using reacted carbon-doped multifilament MgB_2 wires for MRI magnets is reported. To achieve successful superconducting joints, the powder-in-mold method was employed, which involved tuning the filament protection mechanism, the powder compaction pressure, and the heat treatment condition. The fabricated joints demonstrated clear superconducting-to-normal transitions in self-field, with effective magnetic field screening up to 0.5 T at 20 K. To evaluate the interface between one of the MgB_2 filaments and the MgB_2 bulk within the joint, serial sectioning was conducted for the first time in this type of superconducting joint. The serial sectioning revealed space formation at the interface, potentially caused by the volume shrinkage associated with the MgB_2 formation or the combined effect of the volume shrinkage and the different thermal expansion coefficients of the MgB_2 bulk, the filament, the mold, and the sealing material. These findings are expected to be pivotal in developing MgB_2 superconducting joining technology for MRI magnet applications through interface engineering.

Keywords: MgB_2 superconducting joint; MgB_2 conductor; MRI applications; Cryogen-free magnet; Persistent-mode operation.

1. Introduction

Magnetic resonance imaging (MRI) is a medical diagnostic device that helps doctors to examine body organs non-invasively. High-resolution scans of body parts in an MRI are formed using a strong and uniform magnetic field, and radio waves. The powerful and uniform magnetic field needed for forming an MRI scan in an MRI bore is usually generated using several niobium-titanium (Nb-Ti) superconducting coils cooled in expensive liquid-helium (LHe) as schematically shown in Fig. 1(a) [1]. Over the years, helium price has been continuously increasing and supply issues are common [1–5]. High device and installation costs of well over a million dollars and a high maintenance cost restrict smaller diagnostic

* Corresponding authors.
E-mail addresses: dipak.patel@csiro.au (D. Patel), matsumoto.akiyoshi@nims.go.jp (A. Matsumoto).
[1] Current address: The Commonwealth Scientific and Industrial Research Organisation (CSIRO), Lindfield, New South Wales 2070, Australia

https://doi.org/10.1016/j.jma.2023.11.014

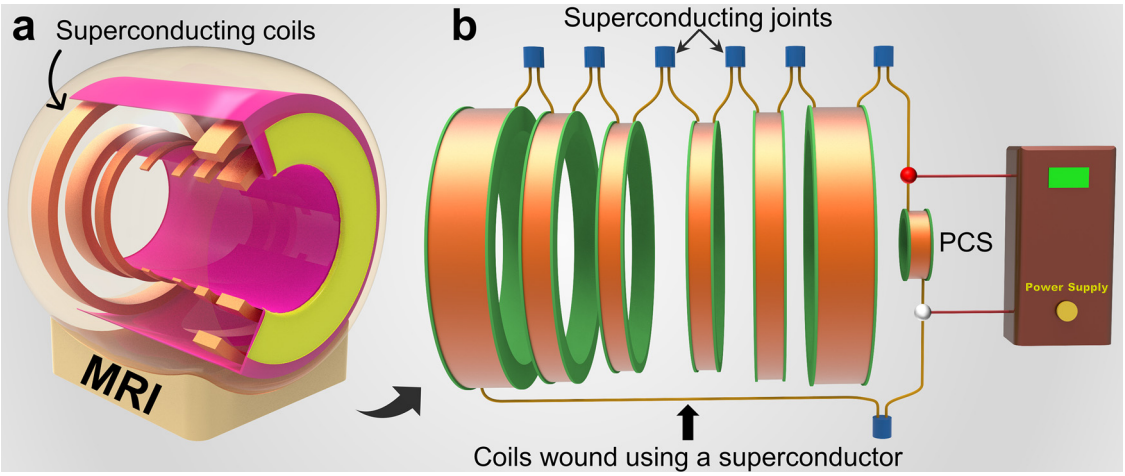

Fig. 1. (a) Artist's 3D model of an MRI scanner. (b) Schematic illustration of a superconducting MRI magnet assembled using multiple superconducting coils, joints, and a PCS.

centers from having an MRI scanner in metropolitan or rural areas [3,6]. Therefore, the development of a cryogen-free cost-effective MRI scanner is crucial for making this critical diagnostic tool widely available to serve communities around the globe.

Philips has made significant progress in this direction by developing a fully sealed magnet known as the BlueSeal magnet which only requires 7 liters (L) of LHe to cool an Nb-Ti MRI magnet at 4.2 K [7]. GE is also developing a similar technology known as Freelium Technology, which is expected to use 20 L of LHe to cool their fully sealed Nb-Ti MRI magnet at 4.2 K [8]. However, to eliminate the requirement to use LHe altogether to cool an MRI magnet, the magnesium diboride (MgB_2) superconductor, which has a critical temperature (T_c) of 39 K is known to be the frontrunner [9–20]. In fact, ASG Superconductor's Paramed MRI unit has developed an MRI scanner using a cryogen-free 0.5 T MgB_2 MRI magnet cooled at 20 K by cryocoolers [21]. Despite the numerous benefits of using an MgB_2 magnet in an MRI [22], the commercial acceptance of the Paramed's MROpen system is still limited [23]. Among several reasons for poor acceptance in the medical industry, one of the reasons could be the mode of operation of its magnet system.

Usually, an Nb-Ti MRI magnet is assembled using multiple coils and each coil is connected with another coil using two *'superconducting joints'* [24], and the ends of the magnet are connected using a persistent-current switch (PCS, a superconducting coil wound in a noninductive fashion) and two superconducting joints to form a closed loop as shown in Fig. 1(b). The PCS allows charging the magnet by inducing a finite resistance across the magnet via an inbuilt heater. Once the magnet is charged and the heater is turned off, the current flows in the closed loop producing the necessary ultra-stable magnetic field (<0.1 ppm h^{-1} decay rate) [1]. This mode of magnet operation is called the persistent-mode operation. The MgB_2 magnet of the Paramed's MROpen MRI scanner is not operated in persistent mode, since the MgB_2 superconducting joining technology has not been fully developed yet. Therefore, the development of superconducting joining technology is crucial for the advancement of MgB_2-based cryogen-free MRI magnets [25].

Since the first report of superconducting joining between an unreacted monofilament MgB_2 wire and an Nb-Ti wire in 2005 [26], many superconducting joints have been fabricated using both monofilament [11,15,27-43] and multifilament MgB_2 conductors [27,29,44-51]. Most of these joints were fabricated using unreacted MgB_2 conductors with few exceptions, in which reacted MgB_2 conductors were used [27,38,45,52]. MgB_2 coils for MRI magnets are expected to be manufactured using a reacted multifilament MgB_2 conductor to minimize modification in the existing manufacturing processes used for Nb-Ti-based MRI magnets [9,53]. This means a superconducting joining technique must be developed that can be used to fabricate joints between reacted multifilament MgB_2 conductors. Moreover, carbon (C)-doped boron (B) powder is often used as a precursor for manufacturing MgB_2 conductors, since C impurity in MgB_2 material helps to improve the performance of MgB_2 conductors in high magnetic fields [14,54-58]. However, a joint fabrication using C-doped MgB_2 conductors is found to be much more difficult compared with un-doped conductors due to unknown reasons [29,33]. Furthermore, the MgB_2-based MRI magnet is expected to be operated at around 20 K to take full advantage of the high cooling capacity of cryocoolers around 20 K. For example, the Cryomech-made single-stage Gifford-McMahon AL630 cryocooler model has a cooling capacity of 100 W at 20 K, whereas their two-stage pulse tube PT450 cryocooler model has a cooling capacity of 5 W at 4.2 K on its 2nd stage and 65 W at 45 K on its 1st stage [59]. No superconducting joint results have been reported to date using reacted C-doped multifilament MgB_2 conductors at 20 K despite the fact that this is the type of MgB_2 conductor that is considered to be nearly fulfilling the requirements for a cryogen-free MRI magnet [9].

To overcome this challenge, for the first time, we report superconducting joints fabricated using reacted C-doped mul-

Table 1
Specifications of the multifilament MgB_2 wire. The multifilament MgB_2 wire used in the study was first heat-treated at 650°C for 1 h before the fabrication of the joints. The joints were then heat-treated for 3 h at 640°C. To compare the performance of the joints with the wire, the wire was heat-treated for a total of 650°C/1h + 640°C/3h before measuring the I_c data.

Specifications	Values
Superconductor	MgB_2
Wire manufacturing method	*In situ*
Doping material, content	Carbon, 2 at%
Sheath, barrier, stabilizer	Monel (Cu + Ni), Nb, Cu
Diameter	0.83 mm
Number of MgB_2 filaments	18
MgB_2 filling factor	12.3%
I_c at 0.5 T, 20 K	96.4 A
Manufacturer	Hyper Tech Research, Inc.

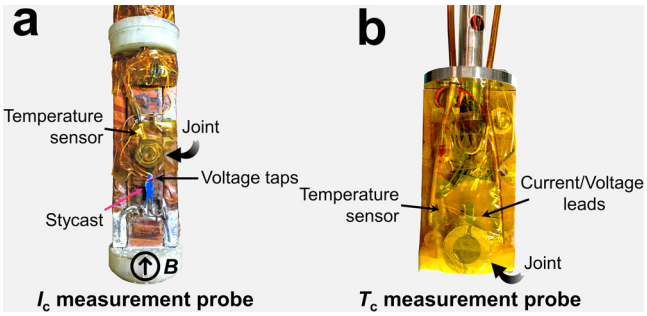

Fig. 2. (a) Photograph of the I_c measurement probe for the joints. (b) Photograph of the T_c measurement probe. The probe was used to measure the resistance of the joint at different temperatures by applying a constant direct current (DC) of 10 mA. The top portion of the joint was cut to fit it within the cryostat's bore.

tifilament MgB_2 wires for MRI magnet applications. To realize a low-temperature reaction between Mg and C-doped B to form an MgB_2 bulk and simultaneous MgB_2 to MgB_2 interface, the powder-in-mold method was employed by concurrently tuning filaments protection mechanism in and out of the mold, the powder compaction pressure, and the heat treatment condition. The fabricated superconducting joints were evaluated in detail for their transport, compositional, and microstructural properties. To further evaluate the interface between one of the MgB_2 filaments and the MgB_2 bulk within the joint, the serial sectioning was carried out for the first time in this type of superconducting joint.

2. Experimental procedures

A multifilament MgB_2 wire (C-doped and *in situ*) for this work was produced using the continuous tube forming and filling (CTFF) process [60]. Table 1 shows the specifications of the MgB_2 wire. A variable temperature insert (VTI) in a superconducting magnet was used to evaluate the critical currents (I_c(s)) of the wire and the joints in different magnetic fields and temperatures. To estimate the I_c(s) of the wire and the joints in a four-probe measurement setup, the criterion of 1 $\mu V\ cm^{-1}$ was utilized. Fig. 2(a) shows the I_c measurement probe for the joints. The T_c of the joint was evaluated by employing the four-probe method in a gas exchange type cryostat. Fig. 2(b) shows the T_c measurement probe.

An X-ray diffraction (XRD) machine, Rigaku Miniflex II was employed to obtain an XRD pattern for the joint's structural analysis; to determine the mole fraction from the XRD data, the Rietveld refinement tool, RIETAN-FP was used [11,61]; for taking scanning electron microscope (SEM) images and energy dispersive X-ray spectroscopy (EDS) maps, a Hitachi SU-70 SEM was used; for focused ion beam (FIB) sample preparation, EDS mapping, the serial sectioning, and SEM images, an FIB-SEM (SMF-1000, Hitachi Hi-Tech Corporation) was used [62].

3. Results and discussion

For fabricating the superconducting joints, the procured MgB_2 wire was first heat-treated at 650°C for 1 h in an in-

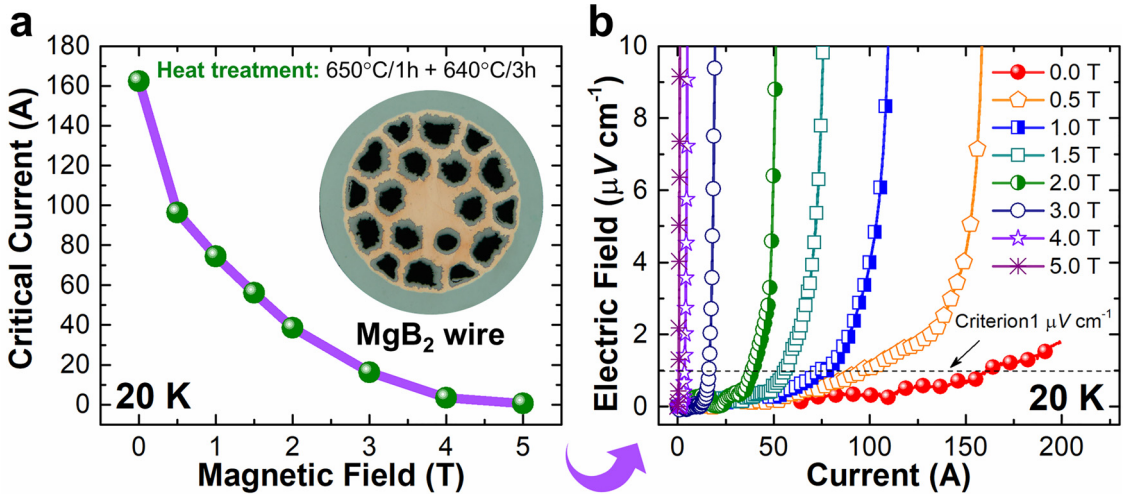

Fig. 3. (a) Critical current of the wire at 20 K in various magnetic fields. Inset: A cross-section of the MgB_2 wire. (b) Current-dependent electric fields at 20 K in various magnetic fields.

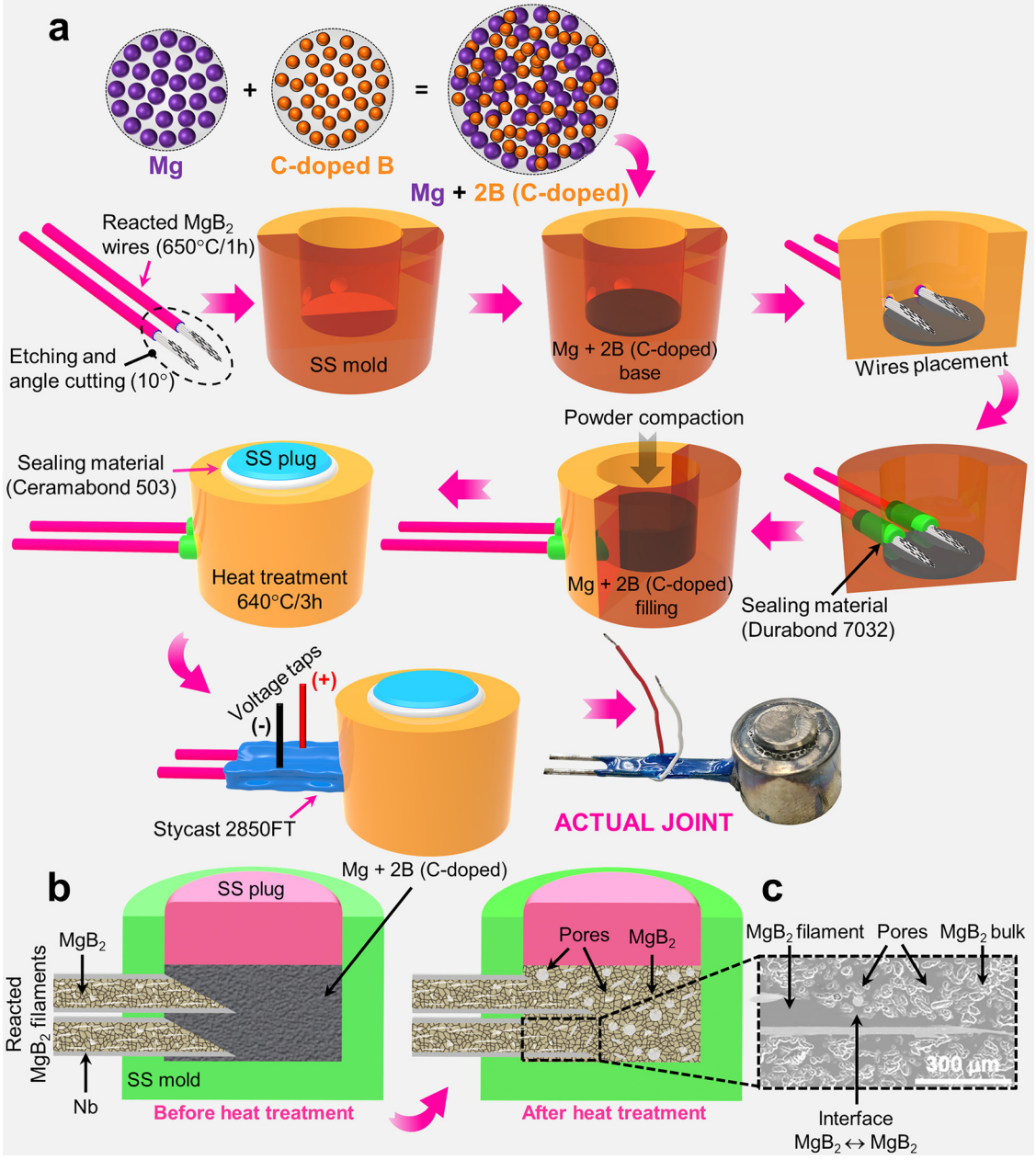

Fig. 4. (a) Joint fabrication steps for reacted C-doped multifilament MgB_2 wires. (b) Joint cross-section illustration before and after the heat treatment. (c) Cross-sectional SEM image of the interface between one of the MgB_2 filaments and the MgB_2 bulk in joint 2. Powder specifications: Mg (Alfa Aesar, 99.8%, −325 mesh) and B (Pavezyum, 4.1 at% C-encapsulated)

ert argon (Ar) atmosphere to form MgB_2 in it. Then, the joints were fabricated using this reacted C-doped multifilament MgB_2 wire. Since the joint fabrication process required the joints to be heat-treated at 640°C for 3 h, the wire was heat-treated for a total time of 650°C/1h + 640°C/3h for measuring the I_c(s). The I_c(s) of the wire at 20 K in various magnetic fields are shown in Fig. 3(a). A cross-section of the MgB_2 wire is shown in the inset. Fig. 3(b) shows the current-dependent electric fields at 20 K in various magnetic fields.

Fig. 4(a) schematically shows our superconducting joining process to connect two reacted C-doped multifilament MgB_2 wires. Copper (Cu) and Monel react with Mg in the course of the heat treatment. Hence, to remove Cu and Monel, nitric acid (HNO_3, 60% w/w, 0.5 h) was utilized to etch the ends of the wires first followed by an angle (10°) cutting [49]. Angle cutting increased the exposed area of the MgB_2 filaments for joining. For wire cutting, an automated cutting machine without any cutting fluid was used (Cutting: 0.64 mm thick diamond disk, Speed: 1 mm min^{-1}, Rotation: 4000 rpm). A stainless steel (SS) mold with two holes on one side was used for the joint fabrication. Table 2 shows the specifications of the mold. In the following step, a base (thickness: ~0.71 mm) was prepared using a mixture of Mg and C-encapsulated B

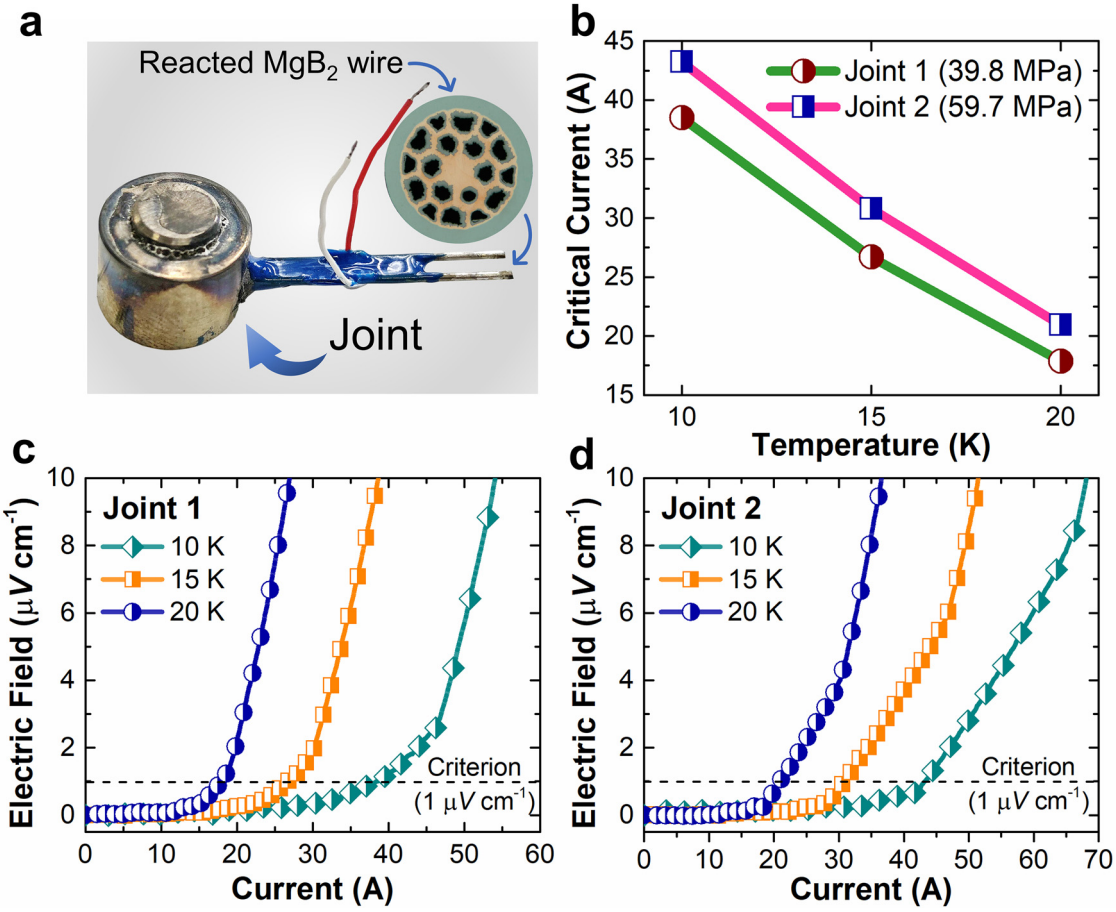

Fig. 5. (a) Photograph of the fabricated superconducting joint using the reacted C-doped multifilament MgB_2 wires. (b) Temperature-dependent critical currents of the joints in self-field. Current-dependent electric fields in self-field at various temperatures of (c) joint 1 and (d) joint 2.

Table 2
Specifications of the mold and the plug.

Specifications	Values
Material	Stainless steel 304L
Diameter of the cavity	8 mm
Height of the cavity	7 mm
Holes dimensions for the insertion of the wires	Diameter: 1.5 mm, 3.5 mm apart
Wall thickness of the mold	3 mm
Diameter/thickness of the plug	7.9 mm/4.5 mm

as per the stochiometric ratio of MgB_2 in an Ar glovebox (compaction pressure: 199 MPa) [49]. In the next step, previously prepared two reacted MgB_2 wires were placed on the base in such a way that only the etched portion of the wires remained inside the mold cavity.

Next, in the open air, Durabond 7032 (a high-temperature sealing material with a maximum operating temperature of 1093°C) [63] was applied inside, in the holes, and outside of the mold to secure the wires. Note that the application of the sealing material inside the mold is crucial to protect the reacted wires from damage due to vertical pressure. The sealant was allowed to cure for 24 h in the open air. After the curing process, the joint was moved to the Ar glovebox, filled using the same Mg + 2B mixture used for the base, and compacted using the specific pressure listed in Table 3. An SS plug was set on the bulk and sealed using Ceramabond 503 (a high-temperature sealing material with a maximum operating temperature of 1650°C) [64]. Following 24 h curing of the sealing material, the joint was heat-treated at 640°C for 3 h in an Ar atmosphere. In all the heat treatment processes, 5°C min^{-1} ramp-up and the cool-down rate were used. Following

Table 3
Specifications of the joints.

Joint	Heat treatment temperature	Wire cutting angle	Compaction pressure for initial Mg + 2B base	Thickness of the initial Mg + 2B bulk	Compaction pressure for the final Mg + 2B bulk
Joint 1	640°C/3h	10°	199 MPa	~0.71 mm	39.8 MPa
Joint 2				~0.71 mm	59.7 MPa

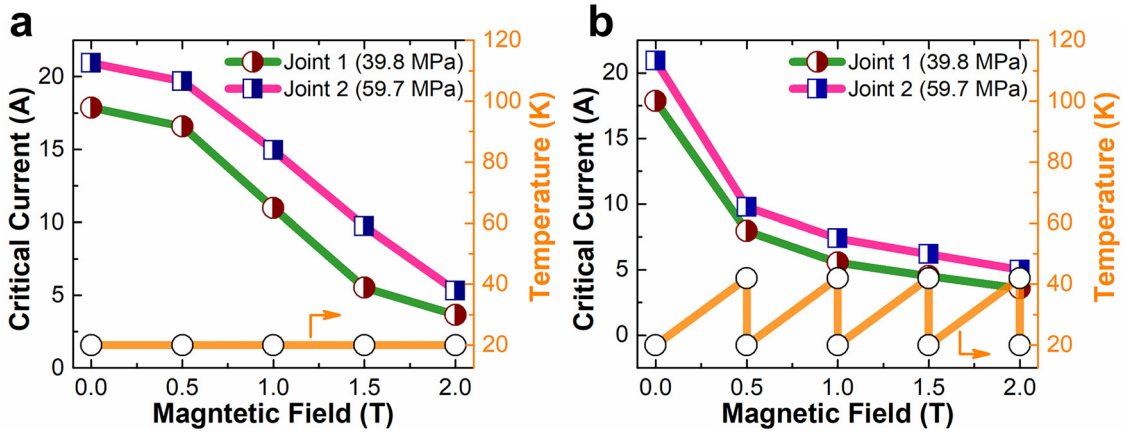

Fig. 6. Magnetic field dependent critical currents of the joints at 20 K. (a) For this I_c(s) measurement, the magnetic field was increased from a low to a high field by keeping a constant temperature of 20 K. (b) For this I_c(s) measurement, the magnetic field was increased from a low to a high field. Before each in-field I_c measurement, the temperature of the joint was raised more than the T_c before cooling down to 20 K.

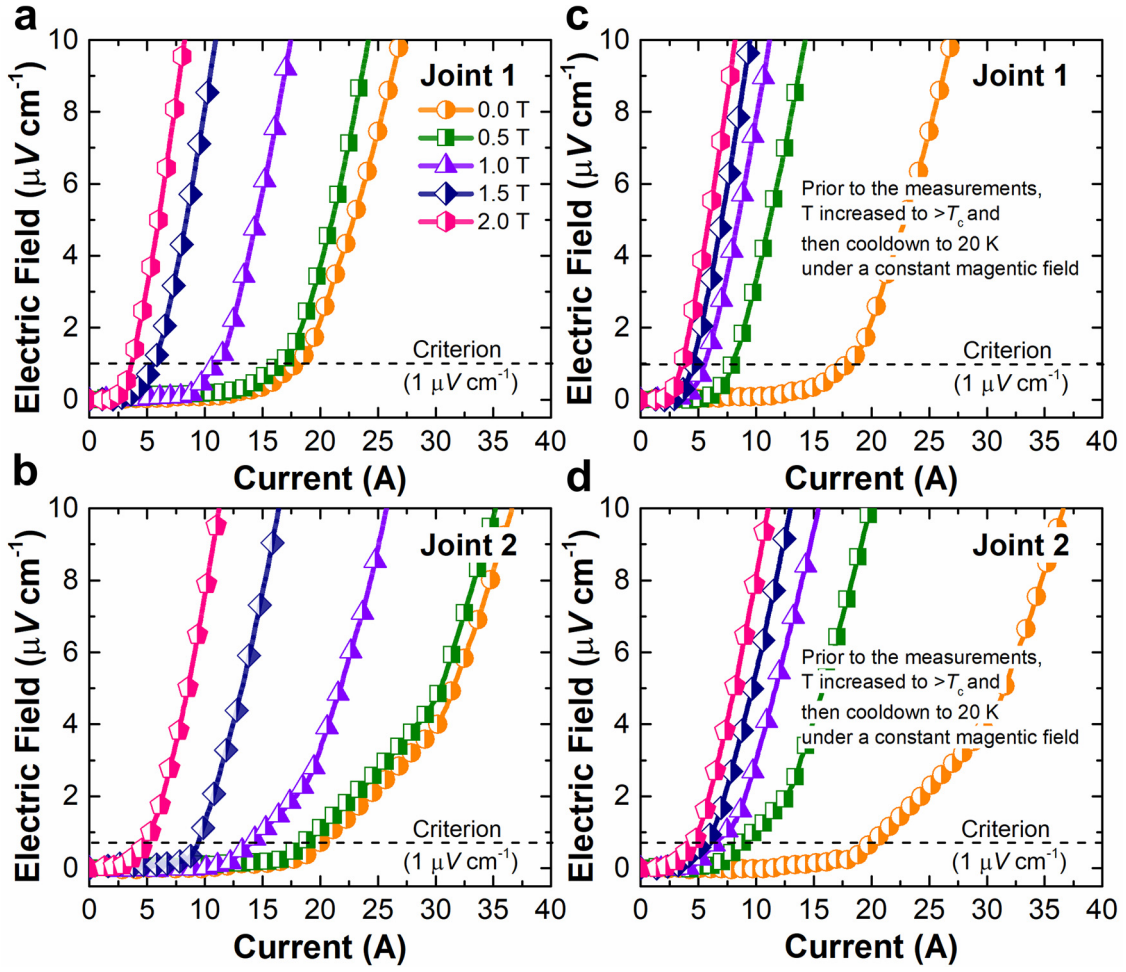

Fig. 7. Current-dependent electric fields of (a) joint 1 and (b) joint 2 at 20 K temperature. For these I_c(s) measurements, the magnetic field was increased from a low to a high field by keeping a constant temperature of 20 K. Electric field versus current characteristics of (c) joint 1 and (d) joint 2 at 20 K temperature. For these I_c(s) measurements, the magnetic field was increased from a low to a high field. Before each in-field I_c measurement, the temperature of the joint was increased beyond the T_c value before cooling down to 20 K.

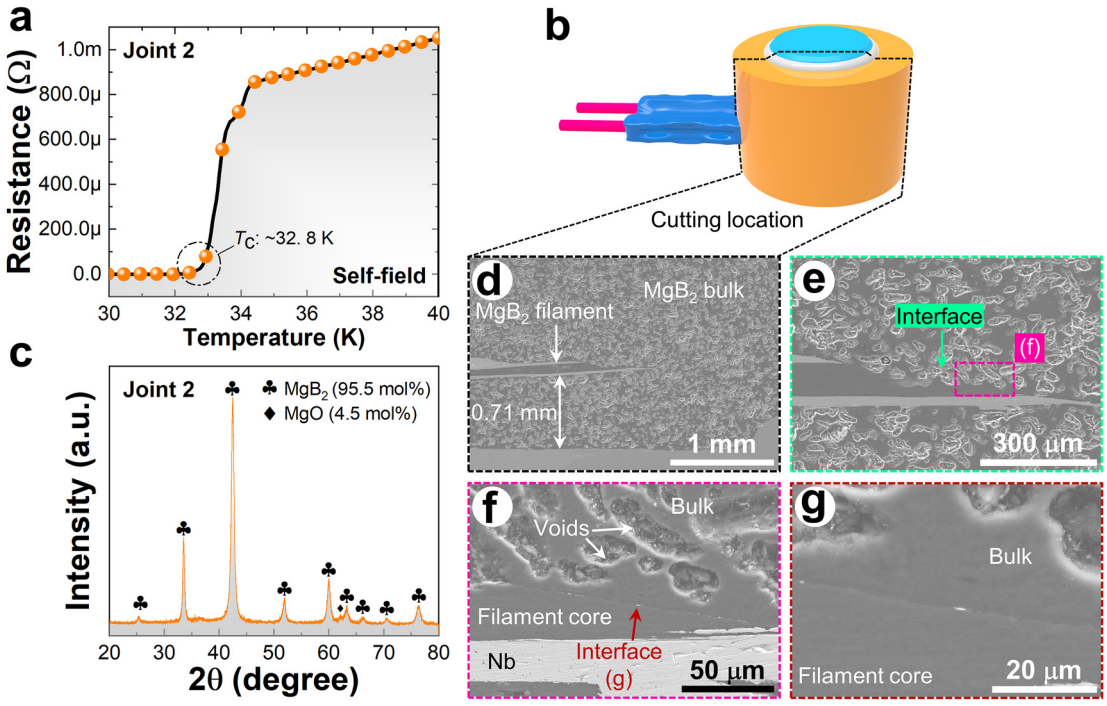

Fig. 8. (a) Relationship between the resistance and temperature for joint 2. (b) A 3D representation of the joint, which indicates the specific location where the joint was cut for subsequent XRD and microscopy studies. (c) XRD pattern for a powder sample obtained from joint 2. SEM images of the interface between one of the MgB_2 filaments within joint 2's cross-section and the MgB_2 bulk taken at different magnifications (d) 40x, (e) 150x, (f) 700x, and (g) 2000x.

the heat treatment of the joint, voltage taps were soldered on the wires. To protect the wires from damage during handling and measurement, Stycast 2850FT prepared using Catalyst 9 was applied and cured for 24 h. Using this method and by applying two different compaction pressures as mentioned in Table 3, two joints (Joint 1: 39.8 MPa, Joint 2: 59.7 MPa) were fabricated. Fig. 4(b) shows the joint cross-section illustration before and after the heat treatment. Fig. 4(c) shows a cross-sectional SEM image of the interface between one of the MgB_2 filaments and the MgB_2 bulk in joint 2. Pores formation was observed in the MgB_2 bulk as a result of diffusion of Mg to B sites.

Fig. 5(a) shows the photograph of the fabricated superconducting joint using the reacted C-doped multifilament MgB_2 wires. Firstly, as shown in Fig. 5(b), the I_c(s) of both joints were measured at various temperatures in self-field. Joint 2 made using 59.7 MPa pressure showed better performance in comparison to joint 1. Joints 1 and 2 reached I_c values of 20.9 A and 17.9 A, respectively at 20 K in self-field. Current-dependent electric fields in self-field at various temperatures of both joints are shown in Figs. 5(c) and 5(d). Clear superconducting-to-normal transitions were observed in both joints at different temperatures.

Once the I_c(s) of the joints were evaluated in self-field, in the next step, the I_c(s) of the joints were evaluated at 20 K in various magnetic fields. Since this type of joint architecture can show the effect of a magnetic field screening as previously reported by us [49], the I_c(s) of the joints were first measured from a low to a high field at 20 K as shown in Fig. 6(a). Corresponding current-dependent electric fields are shown in Figs. 7(a) and (b). As can be seen in Fig. 6(a), both the joints showed a magnetic field screening effect up to 0.5 T, because the reduction in the I_c(s) values were only about 7% and 6% for joints 1 and 2, respectively from self-field to 0.5 T field at 20 K. Beyond 0.5 T, the I_c(s) of the joints were rapidly decreased. The current retention ratio of joint 2 in 0.5 T at 20 K is about 20% compared with the bare wire, which needs improvement for practical applications. Since this is preliminary work, further optimization would be possible to improve the performance of the joints.

To confirm that both joints demonstrated a magnetic field screening effect during the process of measuring the I_c(s) from low to high fields, a different approach was taken in the next step as illustrated in Fig. 6(b). The I_c(s) of the joints were measured by increasing the magnetic field from a low to a high value. However, before each in-field I_c measurement, the joint's temperature was raised above the T_c value and then cooled down to 20 K. As a consequence, some amount of magnetic field was trapped in the joints [49]. Therefore, when the I_c(s) of the joints were re-measured, the reduction in the I_c(s) values was about 44.5% and 46.7% for joints 1 and 2, respectively from self-field to 0.5 T field at 20 K. These findings indicate that both joints exhibited a magnetic field screening effect during the I_c(s) measurements conducted at a constant temperature while increasing the magnetic field from low to high. Current-dependent electric fields for these measurements are shown in Figs. 7(c) and (d).

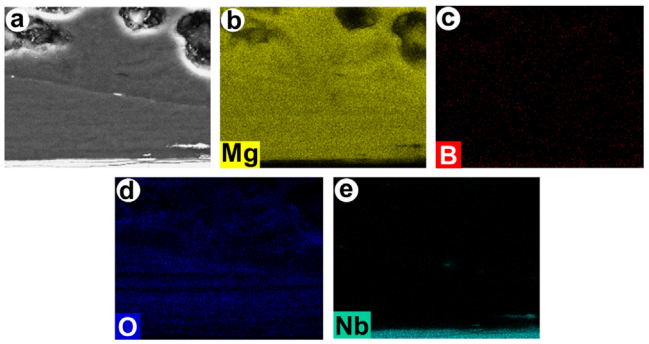

Fig. 9. (a) SEM image of the selected area of interface between one of the MgB_2 filaments and the bulk within joint 2's cross-section (as shown in Fig. 8(g)). EDS maps of (b) Mg, (c) B, (d) O, and (e) Nb acquired from the location shown in Fig. 9(a).

Due to its better performance in comparison to joint 1, joint 2 was selected for further analysis of its T_c in self-field, as illustrated in Fig. 8(a). The measured T_c of joint 2 was ~32.8 K. Reduction in T_c value is usually observed in C-doped MgB_2 material [50]. To further carry out the XRD and microscopy, the joint was cut from a specific location as shown in Fig. 8(b). A half side was used to extract a powder sample for XRD analysis and the other part was used for conducting microscopy. As depicted in Fig. 8(c), an XRD pattern was obtained for a powder sample extracted from joint 2. Despite the presence of the sealing material within the cavity (as shown in Fig. 4(a)), the primary phase identified in the XRD pattern was MgB_2 (95.5 mol%), with a second minor phase of magnesium oxide (MgO, 4.5 mol%). A small amount of MgO formation is common in MgB_2 material due to contamination of Mg during handling [49,53].

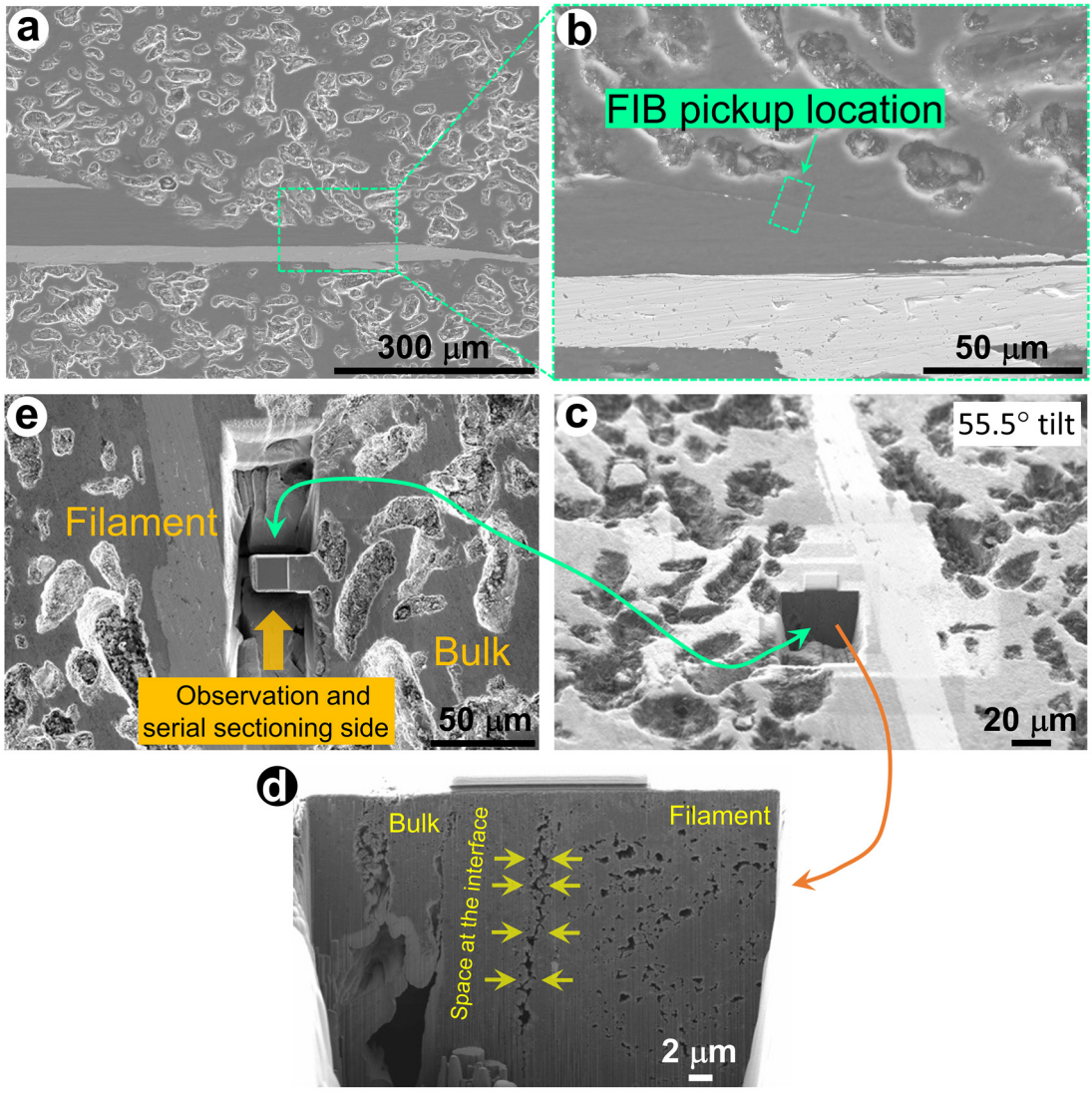

Fig. 10. (a) SEM image of the interface between one of the MgB_2 filaments within joint 2's cross-section and the bulk. (b) SEM image of the selected area is shown in Fig. 10(a) and the FIB pickup location. (c) Tilted (55.5°) SEM image of the interface after removing the material from one side. (d) SEM image of the interface between the MgB_2 bulk and the filament from the location shown via an orange arrow. Space at the interface is marked by several yellow arrows. (e) SEM image of the location from where the interface observation and the serial sectioning were conducted.

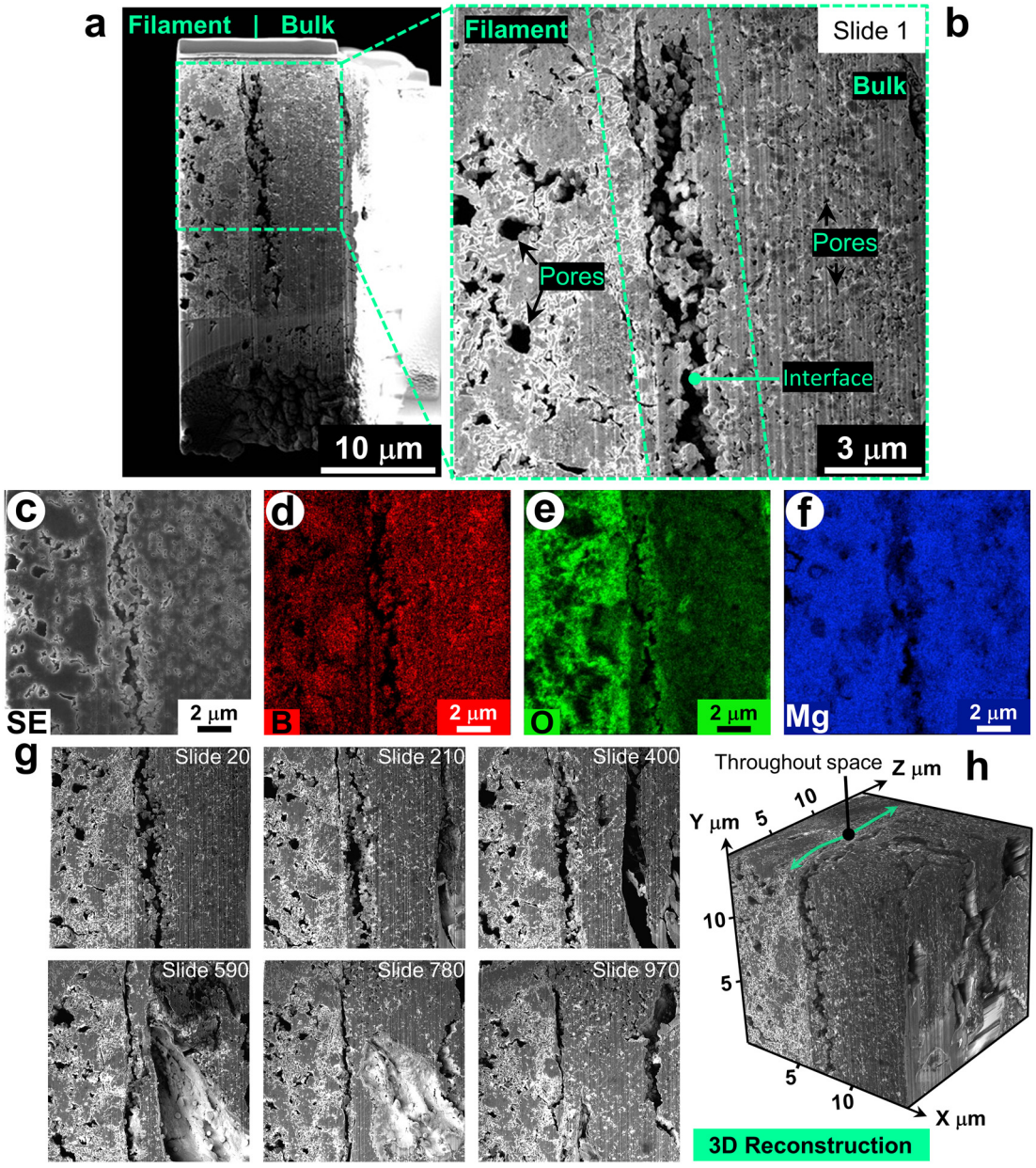

Fig. 11. (a) SEM image of the sample picked up using the FIB from the location shown in Fig. 10(e). (b) SEM image of the area shown in Fig. 11(a). (c) Reference SE image for EDS mapping. EDS maps of (d) B, (e) O, and (f) Mg taken from the area shown in Fig. 11(c). (g) Selected SEM images while performing the serial sectioning using the FIB. Each slide was taken at an average 15.0 ± 0.1 nm depth. (h) 3D reconstructed model from the images taken during the serial sectioning.

After conducting T_c and XRD evaluations, further analysis was performed on the microstructural characteristics of joint 2. SEM images of one of the MgB_2 filaments present within joint 2′s cross-section at varying magnifications are illustrated in Figs. 8(d) to (g). As can be seen in Fig. 8(d), the base height (see Fig. 4(a)) of the MgB_2 bulk was ~0.71 mm. A slightly high magnified SEM image was taken around the MgB_2 filament core and bulk interface as shown in Fig. 8(e). The selected location in Fig. 8(e) was further observed as shown in Fig. 8(f) to see the area around the interface more closely. As can be seen in the figure, many voids were formed in the MgB_2 bulk near the interface. Fig. 8(g) demonstrates that the interface between the filament and bulk of joint 2 appeared to be well-formed, without any noticeable cracks or defects. Corresponding EDS maps of the location shown in Fig. 8(g) are shown in Fig. 9. The defect-free interface implies that the performance of the joint should be much better than what has been measured. To investigate this point further, an FIB was employed to study the cross-section of the interface in the thickness direction.

Figs. 10(a) and (b) illustrate the FIB cutting location to pick up a sample for further analysis. A tilted (55.5°) SEM

image of the interface is depicted in Fig. 10(c) after removing the material from one side, while Fig. 10(d) displays the SEM image of the interface between the MgB_2 bulk and the filament from the indicated location with an orange arrow. The yellow arrows in Fig. 10(d) indicate a visible space at the interface, which is thought to be responsible for the joints' inferior performance. To gain a deeper understanding of the interface, material from the other side was removed using the FIB, as shown in Fig. 10(e). Moreover, SEM, EDS, and the serial sectioning were conducted on the side shown in Fig. 10(e).

Fig. 11(a) shows an SEM image of the sample extracted using the FIB from the interface shown in Fig. 10(e). Fig. 11(b) shows a higher magnification image of the selected area in Fig. 11(a). The left side of the interface represents the MgB_2 filament, while the right side is the MgB_2 bulk. The filament contains a large number of pores compared to the bulk, as shown by black arrows. A visible spacing of up to ~0.98 μm wide can also be observed at the interface. The filament appears to be weakly connected to the bulk at some locations, but clear space is visible in most areas. This spacing could be responsible for the joint's inferior performance.

This space could have potentially formed due to the volume shrinkage (up to 25%) caused by the $Mg + 2B \rightarrow MgB_2$ reaction [65] or the combined effect of the volume shrinkage and the different thermal expansion coefficients (α) of the MgB_2 bulk (41.4×10^{-6} K^{-1} at 20°C and 68.0×10^{-6} K^{-1} at 640°C) [66], the constituent materials of the filament such as Nb (7.0×10^{-6} K^{-1} at 20°C and 8.2×10^{-6} K^{-1} at 640°C) [67] and MgB_2, the stainless steel mold (15.3×10^{-6} K^{-1} at 20°C and 20.6×10^{-6} K^{-1} at 640°C, these properties are of SS304) [68], and the high-temperature sealing material Durabond 7032 (16.2×10^{-6} K^{-1} at room temperature (RT)) [63]. This spacing was likely formed during the reaction process because if it had formed during the cryogenic cooling process, the morphology of the space would be more like a crack. This observation implies that the space was unlikely formed due to the cryogenic epoxy Stycast 2850FT (α of 35.0×10^{-6} K^{-1} at RT) [69] or the high-temperature sealing material Ceramabond 503 (α of 7.2×10^{-6} K^{-1} at RT) [64] pasted on the top of the mold. To improve the joint's performance, this spacing needs to be eliminated.

The interface shown in Fig. 11(c) was further analyzed using EDS mapping as shown in Figs. 11(d) to (f). EDS map of the O shows that O content in the filament was notably high compared with the bulk. This means the filament could have been contaminated during etching using HNO_3. Similar contamination was observed in our previous work [49]. Thus, the etching process must be optimized to minimize contamination to improve the performance of the joint. Furthermore, to observe microstructure in the z-direction, the serial sectioning was conducted. Fig. 11(g) shows selected slides collected during the serial sectioning. A total of 992 slides were collected from a 14.9 μm thickness volume, which resulted in an average slide thickness of 15.0 ± 0.1 nm. As can be seen in the supplemental movie 1 produced using the slides, there is a varying amount of spacing throughout the depth of the specimen. Fig. 11(h) shows the three-dimensional (3D) reconstructed model using the slides. The reconstructed model also shows the spacing throughout. Our findings are expected to play a pivotal role in carrying out interface engineering toward the development of MgB_2 superconducting joining technology for MRI magnet applications.

4. Conclusions

We have successfully fabricated superconducting joints for MRI magnet applications using reacted C-doped multifilament MgB_2 wires for the first time. Our power-in-mold method involves a low-temperature reaction between Mg and C-doped B to form an MgB_2 bulk and simultaneous MgB_2 to MgB_2 interface with the filaments protection mechanism in and out of the mold, the low powder compaction pressure, and 640°C for 3 h heat treatment condition. Joint 2 exhibited an I_c value of 17.9 A at 20 K in 0.5 T, a T_c of ~32.8 K in self-field, and a strong magnetic field screening effect up to 0.5 T at 20 K. The XRD pattern of joint 2 revealed a predominant phase of MgB_2 (95.5 mol%) with a minor MgO (4.5 mol%) phase, despite the presence of sealing material inside the mold cavity. The initial cross-sectional SEM imaging of joint 2 showed a well-formed interface between the filament and the bulk without any visible defects. However, a sample picked up from the interface location using the FIB showed spacing, which was expected to be formed due to the volume shrinkage caused by the $Mg + 2B \rightarrow MgB_2$ reaction or the combined effect of the volume shrinkage and the different thermal expansion coefficients of the MgB_2 bulk, the filament, the mold, and the sealing material. To improve joint performance, this spacing needs to be eliminated.

Declaration of competing interest

The authors declare that they have no known competing financial interests or personal relationships that could have appeared to influence the work reported in this paper.

CRediT authorship contribution statement

Dipak Patel: Conceptualization, Data curation, Formal analysis, Funding acquisition, Investigation, Methodology, Validation, Visualization, Writing – original draft, Writing – review & editing. **Akiyoshi Matsumoto:** Formal analysis, Funding acquisition, Project administration, Resources, Supervision, Validation, Writing – review & editing. **Hiroaki Kumakura:** Validation, Writing – review & editing. **Yuka Hara:** Investigation, Validation, Writing – review & editing. **Toru Hara:** Investigation, Validation, Visualization, Writing – review & editing. **Minoru Maeda:** Formal analysis, Validation, Visualization, Writing – review & editing. **Hao Liang:** Validation, Writing – review & editing. **Yusuke Yamauchi:** Validation, Writing – review & editing. **Seyong Choi:** Validation, Writing – review & editing. **Jung Ho Kim:** Validation, Writing – review & editing. **Md Shahriar A. Hossain:** Funding acquisition, Validation, Writing – review & editing.

Acknowledgement

This work was supported by the Japan Society for the Promotion of Science (JSPS) KAKENHI Grant Number JP18F18714, and Cryogenic Station, Research Network and Facility Services Division, National Institute for Materials Science (NIMS), Japan. This work was also supported by the ARC Linkage Project (LP200200689). The experimental work presented in this manuscript was carried out by Dipak Patel while working at NIMS, Japan, and analyzed at UQ, Australia. The manuscript was organized by Dipak Patel while working at UQ/CSIRO, Australia.

Supplementary materials

Supplementary material associated with this article can be found, in the online version, at doi:10.1016/j.jma.2023.11.014.

References

[1] Y. Lvovsky, E.W. Stautner, T. Zhang, Supercond. Sci. Technol. 26 (2013) 093001.
[2] D. Kramer, Phys. Today 72 (2019) 26–29.
[3] Z.M. Wang, J.M. van Oort, M.X. Zou, Physica C 482 (2012) 80–86.
[4] D. Kramer, Phys. Today 70 (2017) 26–29.
[5] D. Kramer, Phys. Today 2022 (2022) Link: https://pubs.aip.org/physicstoday/Online/5084/Helium-is-again-in-short-supply.
[6] A. Sahu, H. Vikas, N. Sharma, Indian J. Radiol. Imaging. 30 (2020) 190–194.
[7] https://www.philips.com.au/healthcare/resources/landing/the-next-mr-wave/sealed-mr-technology, Date of access: 26/10/23.
[8] https://www.gehealthcare.com/about/newsroom/press-releases/setting-helium-free-revolutionary-mri-tech-ge-healthcare, Date of access: 26/10/23.
[9] M. Parizh, Y. Lvovsky, M. Sumption, Supercond. Sci. Technol. 30 (2017) 014007.
[10] Y. Iwasa, Supercond. Sci. Technol. 30 (2017) 053001.
[11] D. Patel, A. Matsumoto, H. Kumakura, T. Moronaga, Y. Hara, T. Hara, M. Maeda, M.S.A. Hossain, Y. Yamauchi, S. Choi, J.H. Kim, ACS Appl. Mater. Interfaces 13 (2021) 3349–3357.
[12] H. Jie, W. Qiu, M. Billah, M. Mustapic, D. Patel, Z. Ma, D. Gajda, A. Morawski, T. Cetner, M. Shahabuddin, E. Yanmaz, M. Rindfleisch, J.H. Kim, M.S.A. Hossain, Scr. Mater. 129 (2017) 79–83.
[13] H.S. Kim, C. Kovacs, M. Rindfleisch, J. Yue, D. Doll, M. Tomsic, M.D. Sumption, E.W. Collings, IEEE Trans. Appl. Supercond. 26 (2016) 1–5.
[14] M. Maeda, D. Patel, H. Kumakura, G. Nishijima, A. Matsumoto, S.H. Kim, S. Choi, Ceram. Int. 46 (2020) 21752–21756.
[15] V. Braccini, D. Nardelli, R. Penco, G. Grasso, Physica C 456 (2007) 209–217.
[16] T. Baig, A. Al Amin, R.J. Deissler, L. Sabri, C. Poole, R.W. Brown, M. Tomsic, D. Doll, M. Rindfleisch, X. Peng, R. Mendris, O. Akkus, M. Sumption, M. Martens, Supercond. Sci. Technol. 30 (2017) 043002.
[17] D.C. Kara, Production of a viable product in magnetic resonance imaging using MgB_2, Case Western Reserve University, 2014. Master Thesis. (Link: https://etd.ohiolink.edu/acprod/odb_etd/ws/send_file/send?accession=case1386343733&disposition=inline).
[18] D. Patel, M.S. Al Hossain, K.W. See, W. Qiu, H. Kobayashi, Z. Ma, S.J. Kim, J. Hong, J.Y. Park, S. Choi, M. Maeda, M. Shahabuddin, M. Rindfleisch, M. Tomsic, S.X. Dou, J.H. Kim, Supercond. Sci. Technol. 29 (2016) 04LT02.
[19] M. Shahbazi, Y. Hao, D. Patel, H. Liang, Y. Yamauchi, M.S.A. Hossain, J. Magnes. Alloys 10 (2022) 1868–1877.
[20] M.S.A. Hossain, C. Senatore, Y. Yamauchi, M. Mustapic, D. Gajda, D. Patel, A. Khan, J.H. Kim, A.J. Morawski, R. Flukiger, J. Magnes. Alloys 8 (2020) 493–498.
[21] https://www.asgsuperconductors.com/paramed-mri, Date of access: 26/10/23.
[22] D. Patel, M.S. Hossain, W. Qiu, H. Jie, Y. Yamauchi, M. Maeda, M. Tomsic, S. Choi, J.H. Kim, Sci. Rep. 7 (2017) 43444.
[23] A. Ballarino, R. Flukiger, J. Phys. Conf. Ser. 871 (2017) 12098.
[24] D. Patel, S.H. Kim, W. Qiu, M. Maeda, A. Matsumoto, G. Nishijima, H. Kumakura, S. Choi, J.H. Kim, Sci. Rep. 9 (2019) 14287.
[25] G.D. Brittles, T. Mousavi, C.R.M. Grovenor, C. Aksoy, S.C. Speller, Supercond. Sci. Technol. 28 (2015) 093001.
[26] M. Takahashi, K. Tanaka, M. Okada, H. Kitaguchi, H. Kumakura, Supercond. Sci. Technol. 18 (2005) S373–S375.
[27] X.H. Li, L.Y. Ye, M.J. Jin, X.J. Du, Z.S. Gao, Z.C. Zhang, L.Q. Kong, X.L. Yang, L.Y. Xiao, Y.W. Ma, Supercond. Sci. Technol. 21 (2008) 025017.
[28] X. Li, D. Zhang, J. Zhang, Z. Gao, S. Dai, Z. Zhang, D. Xia, G. Zhang, D. Wang, Y. Ma, L. Lin, L. Xiao, IEEE Trans. Appl. Supercond. 21 (2011) 1616–1619.
[29] D.K. Park, J. Ling, M. Rindfleisch, J. Voccio, S. Hahn, J. Bascunan, M. Tomsic, Y. Iwasa, IEEE Trans. Appl. Supercond. 22 (2012) 4400305.
[30] M. Wozniak, B.A. Glowacki, S.B. Setiadinata, A.M. Thomas, IEEE Trans. Appl. Supercond. 23 (2013) 6200104.
[31] J. Ling, J.P. Voccio, S. Hahn, Y. Kim, J. Song, J. Bascunan, Y. Iwasa, IEEE Trans. Appl. Supercond. 25 (2015) 1–5.
[32] D. Patel, M.S. Al Hossain, K.W. See, X. Xu, S. Barua, Z.Q. Ma, S. Choi, M. Tomsic, J.H. Kim, Supercond. Sci. Technol. 28 (2015) 065017.
[33] D. Patel, M.S. Al Hossain, M. Maeda, M. Shahabuddin, E. Yanmaz, S. Pradhan, M. Tomsic, S. Choi, J.H. Kim, Supercond. Sci. Technol. 29 (2016) 095001.
[34] S. Pradhan, S.K. Das, A. Bano, A. Kundu, IEEE Trans. Appl. Supercond. 26 (2016) 1–5.
[35] Y.G. Kim, J.B. Song, J.C. Kim, J.M. Kim, B.H. Yoo, S.B. Yun, D.Y. Hwang, H.G. Lee, Rev. Sci. Instrum. 88 (2017) 086105.
[36] A. Matsumoto, H. Kumakura, IEEE Trans. Appl. Supercond. 28 (2018) 1–4.
[37] Y.H. Choi, Y. Li, D. Park, J. Lee, P.C. Michael, J. Bascunan, J.P. Voccio, Y. Iwasa, H. Tanaka, IEEE Trans. Appl. Supercond. 29 (5) (2019) 4400405.
[38] W.H. Luo, Z.G. Huang, X.W. Cai, X.F. Pan, K.H. Linghu, Q.H. Wu, R.J. Nie, Q.R. Feng, F.R. Wang, Z.Z. Gan, IEEE Trans. Appl. Supercond. 29 (2019) 1–5.
[39] J. Ling, J.P. Voccio, S. Hahn, T. Qu, J. Bascunan, Y. Iwasa, IEEE Trans. Appl. Supercond. 30 (2017) 024011.
[40] H. Tanaka, Y. Li, Y. Choi, D. Park, W. Lee, H. Tanaka, J. Bascunan, Y. Iwasa, IEEE Trans. Appl. Supercond. 31 (2021) 1–5.
[41] H. Liang, D. Patel, M. Shahbazi, A. Morawski, D. Gajda, M. Rindfleisch, R. Taylor, Y. Yamauchi, M.S.A. Hossain, J. Magnes. Alloys 11 (2023) 2217–2229.
[42] I. Husek, P. Kovác, T. Melisek, M. Hain, Ceram. Int. 49 (2023) 11178–11183.
[43] D. Avci, H. Yetis, D. Gajda, M. Babij, L.M. Tran, F. Karaboga, C. Aksoy, A. Zaleski, I. Belenli, Supercond. Sci. Technol. 36 (2023) 75004.
[44] W. Yao, J. Bascunan, S. Hahn, Y. Iwasa, IEEE Trans. Appl. Supercond. 19 (2009) 2261–2264.
[45] D. Nardelli, S. Angius, A. Capelluto, D. Damiani, R. Marabotto, M. Modica, M. Perrella, M. Tassisto, IEEE Trans. Appl. Supercond. 20 (2010) 1998–2001.
[46] B.H. Yoo, J.C. Kim, Y.G. Kim, D.Y. Hwang, J.H. Lee, H.G. Lee, Rev. Sci. Instrum. 89 (2018) 094701.
[47] D. Patel, A. Matsumoto, H. Kumakura, G. Nishijima, M. Maeda, S.H. Kim, S. Choi, J.H. Kim, Scr. Mater. 178 (2020) 198–202.
[48] S.H. Kim, D. Patel, M. Maeda, M. Kim, S.H. Lee, S. Choi, J.H. Kim, Supercond. Sci. Technol. 34 (2021) 125003.

[49] D. Patel, A. Matsumoto, H. Kumakura, M. Maeda, S.H. Kim, H. Liang, Y. Yamauchi, S. Choi, J.H. Kim, M.S.A. Hossain, ACS Appl. Mater. Interfaces 14 (2022) 3418–3426.
[50] D. Patel, A. Matsumoto, H. Kumakura, M. Maeda, S.H. Kim, H. Liang, Y. Yamauchi, S. Choi, J.H. Kim, M.S.A. Hossain, Scr. Mater. 204 (2021) 114156.
[51] D. Xi, D. Wang, C. Xinwei, Q. Wang, Z. Huang, R. Nie, G. Yan, F. Wang, Z. Gan, Supercond. Sci. Technol. 34 (2021) 125009.
[52] L. Xiaohang, Y. Liyang, Z. Dong, W. Dongliang, M. Yanwei, IEEE Trans. Appl. Supercond. 20 (2010) 1528–1531.
[53] D. Patel, A. Matsumoto, H. Kumakura, M. Maeda, S.H. Kim, M.S. Al Hossain, S. Choi, J.H. Kim, J. Mater. Chem. C 8 (2020) 2507–2516.
[54] J.H. Kim, S. Oh, Y.U. Heo, S. Hata, H. Kumakura, A. Matsumoto, M. Mitsuhara, S. Choi, Y. Shimada, M. Maeda, J.L. MacManus-Driscoll, S.X. Dou, NPG Asia Mater 4 (2012) e3.
[55] D. Patel, M.S. Al Hossain, A. Motaman, S. Barua, M. Shahabuddin, J.H. Kim, Cryogenics 63 (2014) 160–165.
[56] Y.W. Ma, X.P. Zhang, G. Nishijima, K. Watanabe, S. Awaji, X.D. Bai, Appl. Phys. Lett. 88 (2006) 072502.
[57] D. Wang, D. Xu, X. Zhang, C. Yao, P. Yuan, Y. Ma, H. Oguro, S. Awaji, K. Watanabe, Supercond. Sci. Technol. 29 (2016) 065003.
[58] S. Ye, H. Kumakura, Supercond. Sci. Technol. 29 (2016) 113004.
[59] https://bluefors.com/products/cryomech-products/, Date of access: 26/10/23.
[60] www.hypertechresearch.com, Date of access: 26/10/23.
[61] F. Izumi, K. Momma, Solid State Phenom 130 (2007) 15–20.
[62] T. Hara, Hitachi Rev 65 (2016) 201–206.
[63] https://www.cotronics.com/WEB%20SHEETS/7032%20color%20wear%20plate%20NP.pdf, Date of access: 26/10/23.
[64] https://www.aremco.com/wp-content/uploads/2015/04/A02_15.pdf, Date of access: 26/10/23.
[65] E.W. Collings, M.D. Sumption, M. Bhatia, M.A. Susner, S.D. Bohnenstiehl, Supercond. Sci. Technol. 21 (2008) 103001.
[66] G. Zhang, C. Xu, M. Wang, Y. Dong, F. Sun, X. Ren, H. Xu, Y. Zhao, Sci. Rep. 11 (2021) 6096.
[67] M.S. Dias, J.R.L.d. Mattos, INAC 2015: International Nuclear Atlantic Conference Brazilian Nuclear Program State Policy for a Sustainable World, 2015 (Link:https://inis.iaea.org/collection/NCLCollectionStore/_Public/47/006/47006411.pdf?r=1).
[68] R.H. Bogaard, P.D. Desai, H.H. Li, C.Y. Ho, Thermochim. Acta 218 (1993) 373–393.
[69] https://datasheets.tdx.henkel.com/LOCTITE-STYCAST-2850FT-en_GL.pdf, Date of access: 26/10/23.